Mass and Heat Transfer Modeling of a Physical Vapor Deposition Effusion Source

S. Tobias Junker
Dept. of Chemical Engineering, University of Delaware, Newark, DE 19716

Robert W. Birkmire
Institute of Energy Conversion, University of Delaware, Newark, DE 19716

Francis J. Doyle III
Dept. of Chemical Engineering, University of California, Santa Barbara, CA 93106

DOI 10.1002/aic.10331
Published online in Wiley InterScience (www.interscience.wiley.com).

The effusion sources modeled in this article are part of a continuous process for production of thin-film photovoltaic modules. Industrial production requires tight control of the vapor flow rates during long run times. A dynamic model is developed to provide physical insight, facilitate simulation studies, and to be incorporated into model-based control schemes. Prediction of the vapor flow rate requires both the mass and energy balance to be solved. Model parameters are estimated based on literature and experimental data, and the entire model is shown to be consistent with independent experimental data. © 2005 American Institute of Chemical Engineers *AIChE J,* 51: 878–894, 2005
Keywords: solar cells, physical vapor deposition, evaporation, free molecular flow, radiative heat transfer

Introduction

Presently, most solar cell systems are based on crystalline silicon technology that is quickly approaching its practical limit in terms of production costs. Thin-film solar cells based on $Cu(InGa)Se_2$ (CIGS) absorber layers are a promising new technology that allows for economical high-volume manufacturing techniques, dramatically reducing costs. These technologies are in a premanufacturing development stage with largely custom-designed equipment and very complex processes.[1]

To date, the highest efficiency thin-film solar cells have been made using CIGS films grown by co-deposition from elemental sources.[2] The approach considered in the present work is the manufacture of CIGS films by deposition onto a flexible substrate using a roll-to-roll processing scheme. The film is deposited by thermal evaporation from a series of elemental sources located sequentially through the deposition zone. The process is semicontinuous with interruptions to change rolls.

A critical issue in commercializing this approach is the maintenance of composition and thickness of the CIGS film at their setpoint over long deposition times. Because of long startup and shutdown times, it is equally important to perform setpoint changes efficiently such that multiple recipes can be tested in a single experiment. In preparation for advanced process control design, efforts to model the thermal effusion sources are described in this paper. The dynamic model provides physical insight, facilitates simulation studies, and can be incorporated into model-based controllers.

Process description

The process (see schematic in Figure 1) can be divided into two subsystems: (1) the effusion subsystem and (2) the deposition subsystem. The effusion subsystem consists of the elemental sources for copper, gallium, and indium, where electric

Correspondence concerning this article should be addressed to F. J. Doyle III at doyle@engineering.ucsb.edu.

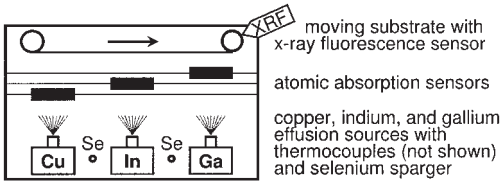

Figure 1. Schematic of the deposition chamber.

The four main parts are (1) effusion sources for copper, indium, and gallium with internal thermocouples; (2) an atomic absorption sensor for each source; (3) a sparger for selenium; and (4) the moving substrate with X-ray fluorescence sensor.

energy to resistive heaters is supplied as the input, and the outputs are temperature and absorbance measured by thermocouples and atomic absorption spectroscopy sensors for each source. Selenium is provided in excess and assumed to react stoichiometrically. The atomic absorption sensors measure the vapor flow rate based on the attenuation of an element-specific sample beam. An additional reference beam, which is not element specific, allows for correction of the measurement.

The deposition subsystem consists of the moving substrate to which the elemental vapor fluxes are delivered as the input and the outputs are the final film thickness and composition measured by X-ray fluorescence (XRF). The XRF sensor was developed at ITN Energy Systems in Littleton, CO and Global Solar Energy in Tucson, AZ.[3] See Junker et al.[4] for development of a fundamental model and analysis of model-based control strategies for the deposition subsystem. In this control strategy, the deposition subsystem's controller provides flow rate setpoint trajectories for the effusion subsystem. Maintaining these flow rate setpoints requires advanced process control, which in turn necessitates the process model described herein.

Each effusion cell (see schematic in Figure 2) is resistively heated to first melt and evaporate the metal. The crucible is covered by a lid with two nozzles. The cell's subunits are made from boron-nitride (lid, crucible, heater support) and graphite (heater, crucible support). The crucible is filled with melt and a thermocouple is located in its base.

Overview

The article is organized in four main sections. The starting point is the *mass transfer model*, which describes the dynamics of melting and evaporation as well as constitutive equations predicting the vapor flow rate. Directly related to the mass transfer model is the *atomic absorption sensor model*, which predicts the absorbance as a function of the vapor flow rate. To predict melting and evaporation, knowledge of the heat flow into the melt and the melt temperature is required. This constitutes the theme of the *heat transfer model*, which predicts the temperatures of the effusion cell's subunits, and the energy flows among them as a function of the electric energy input. Next, model parameters are estimated based on data from both the literature and from specific identification experiments. Finally, the overall heat and mass transfer model's consistency is crosschecked with novel experimental data that are different from the data used for parameter estimation.

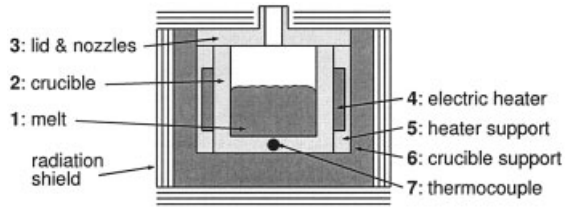

Figure 2. Schematic cross section of effusion cell.

The cells for copper, gallium, and indium are identical. The radiation shield consists of layers of stainless steel foil and graphite felt.

Table 1. Regimes of Mass Balance

Regime	Temperature	Mass	Energy
1	$T_1 \neq T_m$		
2	$T_1 = T_m$	$m_s > 0$	$\dot{Q}_1 < 0$
3	$T_1 = T_m$	$m_t - m_s > 0$	$\dot{Q}_1 > 0$

Mass-Transfer Model

Mass balance

To describe both reduction of total mass arising from evaporation and phase changes resulting from melting and solidification, mass balances are formulated for both the total mass m_t and the solid mass m_s. Neglecting sublimation from the solid phase, three regimes can be distinguished: (1) heating, cooling, and evaporation; (2) melting; and (3) solidification. The regimes, which depend on the melting point T_m, the net energy flow $\dot{Q}_1$ leaving the melt, the melt temperature T_1, and the amounts of total and solid mass, are summarized in Table 1.

The differential equations describing the change of solid and total mass are given as follows

$$\frac{dm_s}{dt} = \begin{cases} 0 & \text{regime 1} \\ \dot{Q}_1/\Delta\hat{H}^{\text{fus}} & \text{regimes 2 and 3} \end{cases} \tag{1}$$

$$\frac{dm_t}{dt} = -\dot{m}_{\text{vap}}(T_{\text{melt}}) \tag{2}$$

where $\Delta\hat{H}^{\text{fus}}$ is the mass specific heat of fusion, $\dot{m}_{\text{vap}}$ is the evaporation flow rate, and T_{melt} is the melt temperature. Computation of $\dot{Q}_1$ and T_{melt} is the subject of the heat transfer model. The remainder of this section focuses on the constitutive equations describing the evaporation from a surface and the low-pressure flow through a nozzle.

Evaporation flow rate

The vapor flow $\dot{m}_{\text{vap}}$ from the melt surface A_{melt} is proportional to the difference in vapor pressure p_{vap} and the cell pressure p_{cell} above the surface. It is described by the Hertz–Knudsen equation[5]

$$\frac{\dot{m}_{\text{vap}}}{A_{\text{melt}}} = \eta_v \frac{p_{\text{vap}} - p_{\text{cell}}}{\sqrt{2\pi RT/M}} \tag{3}$$

where T is the absolute surface temperature; M is the molecular weight; R is the ideal gas constant; and η_v the evaporation coefficient, defined as the ratio of observed to theoretically possible evaporation flow. Values of $\eta_v < 1$ are attributable to

surface contamination.[5] Because only high-purity raw materials are used (99.999%), η_v is assumed to be unity.

Because the cell pressure is unknown, additional equations describing the vapor flow through the nozzle are required. Although Eq. 3 is of general validity, flow through the nozzle depends on the flow regime that is defined by the value of the Knudsen number (Kn)

$$\mathrm{Kn} = \frac{\lambda_m}{2\Gamma} \tag{4}$$

where λ_m is the mean free path and Γ is the nozzle radius. Three flow regimes are commonly defined[6]: (1) free molecular (Kn $>$ 1), where molecule–wall collisions dominate; (2) transitional ($0.01 \leq \mathrm{Kn} \leq 1$); and (3) viscous (Kn $<$ 0.01), where molecule–molecule collisions dominate.

In the current situation, flow equations for the free molecular and the transitional regimes are needed. On-line computation of the flow rate as a function of temperature is an iterative process, given that (a) the flow regime depends on the Knudsen number, but (b) the Knudsen number is computed based on mass flow and pressure, which are computed in (a). To avoid iterations, the flow equations are solved for mass flow and pressure for a wide range of melt temperatures and then the proper flow regime is selected.

Mean Free Path and Viscosity. To determine the proper flow regime, the mean free path λ_m is required. The classic result from kinetic theory is (see Eq. 106d in Kennard[7])

$$\lambda_m = \frac{k_b T}{\sqrt{2}\ \pi\sigma^2 p} \tag{5}$$

where k_b is Boltzmann's constant and σ is the collision diameter. As an estimate of σ, the van der Waals diameter was used.

A better estimate of λ_m can be obtained by using a relationship between viscosity and mean free path because the deviation from rigid sphere behavior can be accounted for in the computation of viscosity. Such a relationship, given by Kennard[7] (see Eq. 126b therein), can be written as

$$\lambda_m = \sqrt{\frac{\pi RT}{1.992M}}\,\frac{\mu}{p} \tag{6}$$

where μ is the dynamic viscosity. From a rigorous kinetic approach for pure substances and only binary collisions (see p. 23 in Hirschfelder et al.[8]), it is given by

$$\mu = \frac{5}{16}\ \sqrt{\frac{k_b}{N_A\pi}}\,\frac{\sqrt{MT}}{\sigma^2\Omega_\mu} \tag{7}$$

which is also known as the Chapman–Enskog equation.[9] Here, N_A is the Avogadro constant and Ω_μ accounts for the deviation from rigid sphere behavior. Ω_μ is tabulated (see Table B-2 in Bird et al.[9]) as a function of the dimensionless temperature k_bT/ε, where ε is the maximum energy of attraction between a pair of molecules.

Bird et al.[9] (see p. 22 therein) give an empirical relationship for the value of ε as a function of the melting point

$$\varepsilon/k_b = 1.92T_m \tag{8}$$

Over the temperature range of interest, the value of Ω_μ varies between 2 and 3 such that there is a clear deviation from rigid sphere behavior.

Free Molecular Flow. By using the kinetic theory of gases, Brown et al.[10] give the following relationship for flow through the nozzle in the free molecular regime:

$$\frac{\dot{m}_{\mathrm{nozz}}}{A_{\mathrm{nozz}}} = K(\Lambda)\,\frac{p_{\mathrm{cell}} - p_{\mathrm{chamb}}}{\sqrt{2\pi RT/M}} \tag{9}$$

where A_{nozz} is the nozzle cross section, $\Lambda = L/\Gamma$ is the nozzle aspect ratio, and p_{chamb} is the chamber pressure. Kennard[7] (see pp. 307–308ff. therein) gives a relationship for K as a function of the aspect ratio

$$\Lambda \leq 1.5 \quad : \quad K(\Lambda) = \frac{1}{1 + 0.5\Lambda} \tag{10}$$

$$\Lambda > 1.5 \quad : \quad K(\Lambda) = \frac{1 + 0.4\Lambda}{1 + 0.95\Lambda + 0.15\Lambda^2} \tag{11}$$

The limiting cases are an ideal orifice ($\Lambda = 0$) with $K = 1$ and a long pipe ($\Lambda \to \infty$) with $K = (\pi/2)[2/f - 1]/\Lambda$.[10]

Because the vapor flow is divided between two nozzles, the mass continuity equation is

$$\dot{m}_{\mathrm{vap}} = 2\dot{m}_{\mathrm{nozz}} \tag{12}$$

Neglecting the chamber pressure ($p_{\mathrm{chamb}} \approx 10^{-7}$ torr $= 1.3 \times 10^{-10}$ bar), Eqs. 3, 9, and 12 can now be solved for $\dot{m}_{\mathrm{vap}}$

$$\frac{\dot{m}_{\mathrm{vap}}}{A_{\mathrm{eff}}^{\mathrm{free}}} = \frac{p_{\mathrm{vap}}}{\sqrt{2\pi RT/M}} \tag{13}$$

where

$$\frac{1}{A_{\mathrm{eff}}^{\mathrm{free}}} = \frac{1}{\eta_v A_{\mathrm{melt}}} + \frac{1}{2K(\Lambda)A_{\mathrm{nozz}}} \tag{14}$$

is the effective transport cross section for free molecular flow. The cell pressure p_{cell} follows then from Eq. 3. The mean free path, needed when determining the Knudsen number, should be computed at the mean pressure p_m^{free} within the nozzle[10]

$$p_m^{\mathrm{free}} = \frac{p_{\mathrm{cell}} + p_{\mathrm{chamb}}}{2} = \frac{p_{\mathrm{cell}}}{2} \tag{15}$$

Transitional Flow. In the transitional flow regime, the two-equation approach of Brown et al.[10] (see pp. 810–812 therein) takes entrance effects at the nozzle into account

$$\frac{\dot{m}_{\mathrm{entr}}}{A_{\mathrm{nozz}}} = B\,\frac{p_{\mathrm{cell}} - p_{\mathrm{entr}}}{\sqrt{2\pi RT/M}} \tag{16}$$

$$\frac{\dot{m}_{\text{nozz}}}{A_{\text{nozz}}} = \frac{\Gamma^2}{16\mu L}\frac{p_{\text{entr}}^2 - p_{\text{chamb}}^2}{RT/M}\left[1 + 4\left(\frac{2}{f} - 1\right)\frac{\lambda_m}{\Gamma}\right] \quad (17)$$

In the first equation, B is a correction factor to account for entrance losses, and p_{entr} is the pressure at the nozzle entrance. The second equation[10] (see Eq. 7 therein) is based on the equation for compressible viscous flow in a pipe[10] (see Eq. 1 therein). Here, L is the nozzle length and f is the fraction of molecules diffusively reflected from the wall. The term in square braces is a correction factor describing slip flow occurring at low pressures (see p. 802 in Brown et al.[10]).

Using the continuity equation

$$\dot{m}_{\text{vap}} = 2\dot{m}_{\text{entr}} = 2\dot{m}_{\text{nozz}} \quad (18)$$

p_{cell} can be eliminated from Eqs. 3 and 16 to obtain

$$\frac{\dot{m}_{\text{vap}}}{A_{\text{eff}}^{\text{trans}}} = \frac{p_{\text{vap}} - p_{\text{entr}}}{\sqrt{2\pi RT/M}} \quad (19)$$

where

$$\frac{1}{A_{\text{eff}}^{\text{trans}}} = \frac{1}{\eta_\iota A_{\text{melt}}} + \frac{1}{2BA_{\text{nozz}}} \quad (20)$$

is the effective transport cross section for transitional flow. The mean pressure p_m^{trans} within the nozzle is

$$p_m^{\text{trans}} = \frac{p_{\text{entr}} + p_{\text{chamb}}}{2} = \frac{p_{\text{entr}}}{2} \quad (21)$$

Using Eq. 6 with $p = p_m^{\text{trans}}$, Eq. 17 can be written as

$$\frac{\dot{m}_{\text{nozz}}}{A_{\text{nozz}}} = \frac{\Gamma^2}{16\mu L}\frac{M}{RT}\left(1 + \frac{p'}{p_{\text{entr}}}\right)p_{\text{entr}}^2 \quad (22)$$

where

$$p' = \frac{8\mu}{\Gamma}\left(\frac{2}{f} - 1\right)\sqrt{\frac{\pi RT}{1.992M}} \quad (23)$$

Using Eq. 18, the mass flow can now be eliminated from Eqs. 19 and 22 to get

$$p_{\text{entr}}^2 + (p' + p'')p_{\text{entr}} - p''p_{\text{vap}} = 0 \quad (24)$$

where

$$p'' = \frac{8\mu L}{\Gamma^2}\sqrt{\frac{RT}{2\pi M}}\frac{A_{\text{eff}}^{\text{trans}}}{A_{\text{nozz}}} \quad (25)$$

and p_{entr} is the positive solution of the quadratic Eq. 24, such that

$$p_{\text{entr}} = -\frac{p' + p''}{2} + \sqrt{\frac{(p' + p'')^2}{4} + p''p_{\text{vap}}} \quad (26)$$

The mass flow follows then from Eq. 19 and the cell pressure from Eq. 3. The mean free path, needed when determining the Knudsen number, should be computed at the mean pressure p_m^{trans}.

Parameter Fit for Copper. Depending on the Knudsen number, evaporation occurs either in the free molecular or in the transitional flow regime. Flow in the free molecular regime is described by Eq. 13 and has no unknown parameters. Flow in the transitional regime, as described by Eqs. 16 and 17, depends on the parameters B and f.

For flow situations similar to the current case, a value of $f = 0.9$ has been reported in the literature.[6,10] A value of B that minimizes the sum-squared error between the predicted and experimental flow rates is determined by nonlinear optimization using the *fmincon* command from Matlab's Optimization Toolbox.[11] For copper, an optimal fit is obtained for $B = 1.09$. For these values of B and f, the maximum deviation between measurements and prediction is 6.4 g/h; the mean of the absolute deviation is 2.8 g/h.

Over a certain temperature region (for copper, 1393–1492°C), neither regime is valid. In that region, the Knudsen number computed assuming validity of the free molecular flow result (see Eq. 13) is <1, and the Knudsen number computed assuming validity of the transitional flow result (see Eq. 26) is >1. Therefore, interpolation between the two flow regimes is necessary.

Most conveniently, interpolation is accomplished by extrapolating one of the flow regimes. Because the free molecular flow equations have a more fundamental basis than the transitional (that is, no assumptions regarding slip flow and entrance effects), extrapolation of the free molecular regime is preferred. Coincidentally, for the optimal values of f and B, the extrapolation of the free molecular regime joins the transitional regime with almost identical value (0.24% deviation) and slope (5.5% deviation), such that no further adjustment of B is necessary (see Figure 3).

Lacking experimental data for indium and gallium, evaporation profiles based on the same values $f = 0.9$ and $B = 1.09$ are used (see Figure 4). The evaporation characteristics for all three elements can thus be generated off-line and stored in a look-up table for fast access during simulations.

Atomic absorption sensor model

Arranged within the chamber are Luxtron® ATOMICAS™ atomic absorption (AA) sensors that measure the effusion flux by attenuation of an element-specific light beam. Based on the Lambert–Beer law[12] (see pp. 428ff therein) Hanket[13] (see Eq. 10.16 therein) developed a model that relates $\dot{m}_{\text{vap}}$ to the absorbance α, as follows

$$\alpha = 100(1 - x_\beta)\left[1 - \exp\left(-\kappa\gamma\sqrt{\frac{\pi M}{8RT}}\dot{m}_{\text{vap}}\right)\right] \quad (27)$$

where x_β is the fraction of noninteracting photons; κ is the mass extinction coefficient, which is a measure for the light attenuation; and γ is a geometric constant that stems from a path integration of the vapor flux distribution (see Eq. 10 in Junker et al.[4]). For copper, Hanket[13] (see p. 359 therein) estimated a

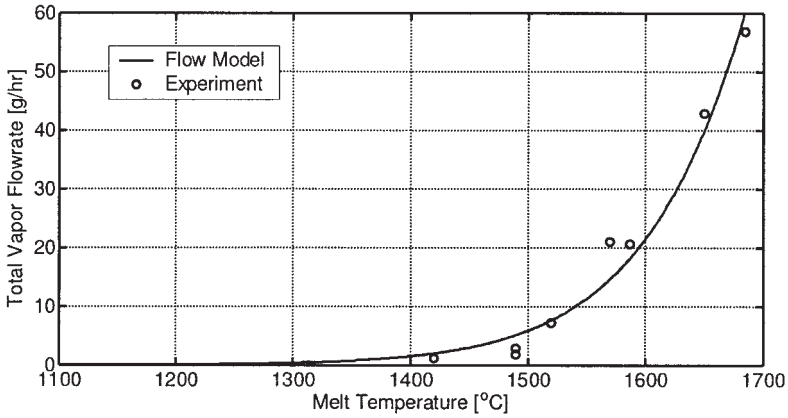

Figure 3. Parameter fit of flow equations for copper.

value of $x_\beta = 0.16$. To predict either sensor measurements or flow rates, the product $\kappa\gamma$ has to be estimated based on experimental data.

Heat-Transfer Model

Simplifying assumptions

The general three-dimensional transient heat transfer problem is very complicated. To develop a model that is numerically tractable and thus useful for on-line computation by a controller, several simplifying assumptions are made:

(1) The effusion source can be divided into subunits i (see Figure 2). For each subunit, it is assumed that

(a) its temperature T_i is uniform. This lumped capacitance assumption is valid for small Biot numbers (see below).

(b) its specific heat capacities at constant volume $c_{v,i}$ and constant pressure $c_{p,i}$ are approximately equal, which is valid for liquids and solids.

(c) its density ρ_i is independent of T_i and thus constant. If data were available, this assumption could easily be relaxed.

(2) For each contact surface between the subunits i, it is assumed that

(a) it is opaque and thus does not transmit radiation.

(b) its radiation is independent of direction (diffuse), which is a reasonable assumption for many surfaces (see p. 657 in Incropera and DeWitt[14]).

(c) its emissivity is independent of wavelength (gray), which is a necessary assumption because of lack of better data.

(d) the heat and mass fluxes leaving the surface are uniform across the surface. Given assumption (1a), this is valid as long as the material properties are uniform.

(3) The thermocouple has a sufficiently small mass so that it does not influence the crucible's temperature.

(4) Radiative coupling between the effusion sources can be neglected because the radiation shield's outside temperatures are significantly less than the cell's inside temperatures.

(5) The vapor inside the crucible does not participate in the radiation exchange, which is justified because it is a nonpolar gas (see p. 749 in Incropera and DeWitt[14]) at a very low pressure (for copper, $p_{\text{cell}} = 9 \times 10^{-5}$ bar at $T_1 = 1400°\text{C}$).

(6) Potential and kinetic energies can be neglected, which is valid given that the system is stationary without any moving parts.

(7) Viscous dissipation can be neglected because only free and Marangoni convection occurs in the melt (see below).

For validity of the lumped capacitance assumption, a Biot number (Bi) < 0.1 is required (see pp. 212–220 in Incropera and DeWitt[14]), which is defined as the ratio of external heat transfer coefficient h and internal thermal conductivity k

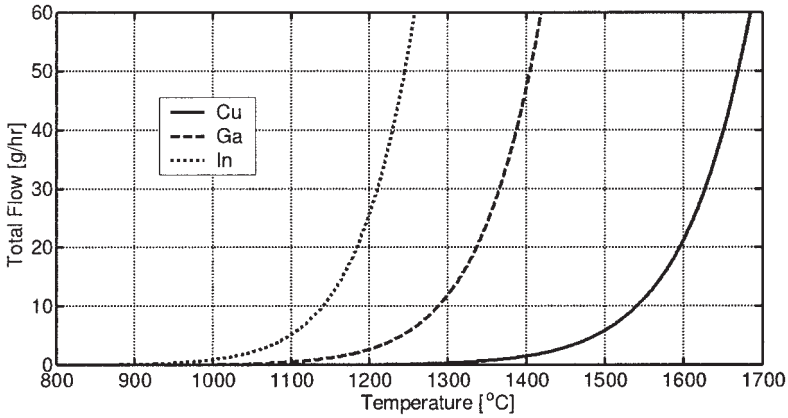

Figure 4. Prediction of total flow rate for copper, gallium, and indium using $f = 0.9$ and $B = 1.09$.

$$\mathrm{Bi} = \frac{hL_c}{k} \tag{28}$$

where L_c is a characteristic dimension.

Because external heat transfer occurs by a combination of conduction, convection, and radiation, an effective heat transfer coefficient h^{eff} is defined based on the cumulative heat flow $\dot{Q}$ for each subunit

$$\dot{Q} = h^{\mathrm{eff}} A (T - T_{\mathrm{sur}}) \tag{29}$$

where A is the heat exchange area, and T and T_{sur} are the absolute temperatures of the subunit and its surroundings, respectively. Because of the temperature and heat flow dependency of h^{eff}, consistency of the lumped capacitance assumption can be verified only after a result has been obtained (see *Biot number*).

Energy balance

Based on assumptions 1–7 above, the general energy balance for a control volume V fixed in space (for example, see p. 458 in Bird et al.[9]) simplifies to an ordinary differential equation for each subunit i

$$\frac{dT_i}{dt} = -\frac{\dot{Q}_i + P_i + \dot{m}_i \Delta \hat{H}_i^{\mathrm{vap}}}{m_i \left(c_{p,i} + T_i \dfrac{dc_{p,i}}{dT} \right)} \tag{30}$$

where $\dot{Q}_i$ is the total heat leaving component i and $\Delta \hat{H}_i^{\mathrm{vap}}$ is the mass specific heat of vaporization. For the melt, $\dot{m}_1$ is the vapor flow rate as a function of T_1, for the other subunits, $\dot{m}_i$ is zero. For the resistive heater, P_4 is the supplied electric power; for the other subunits, P_i is zero.

Energy flow rates

To complete the energy balance, the remainder of this section focuses on the constitutive equations describing the conductive, convective, and radiative heat flows among the effusion cell's subunits.

Resistive Heater. Each effusion source is driven by a silicon-controlled rectifier (SCR) power supply with a maximum output of $P_{\max} = 2$ kW. The provided power is proportional to the control move u (0–100%). The heater is modeled phenomenologically by a simple linear relationship. To account for losses, an efficiency η_{el} has been introduced such that the heater model becomes

$$P_4 = \eta_{\mathrm{el}} P_{\max} \frac{u}{100} \tag{31}$$

The efficiency cannot easily be determined by measuring the current or voltage supplied to the heater because the SCR's signal is neither sinusoidal nor periodic.

Conduction among Subunits of the Effusion Source. Among the subunits of the effusion source, heat transfer is limited by the contact resistance between the subunits, that is, at the graphite/boron-nitride and boron-nitride/boron-nitride interfaces. Phenomenologically, the cumulative heat transfer between subunit i and its neighboring subunits can be modeled as

$$\dot{Q}_i^{\mathrm{cond}} = \sum_j C_{ij} A_{ij} (T_i - T_j) \tag{32}$$

where A_{ij} is the contact area and C_{ij} is the contact conductance. Although the subunits have a tight fit, the inevitable vacuum gaps will result in small conductances. Based on data in the literature (see Table 3.1 in Incropera and DeWitt[14]), values of $C_{ij} < 2000$ W m^{-2} K^{-1} are expected.

Convection between Melt and Crucible. Because of the effusion cell's design, the front side wall is hotter than the back side wall. In this situation, two modes of convection occur: (1) free convection attributed to density gradients[15,16] and (2) Marangoni convection attributed to gradients in the surface tension at the melt/gas interface.[17,18] Phenomenologically, this can be expressed as

$$\dot{Q}_{12}^{\mathrm{conv}} = U_{12}^{\mathrm{conv}} A_{12} (T_1 - T_2) \tag{33}$$

Based on data in the literature (see Table 1.1 in Incropera and DeWitt[14]), values of $U_{12}^{\mathrm{conv}} < 5000$ W m^{-2} K^{-1} are expected.

Radiation. Heat transfer by radiation occurs among the cell's components; among the effusion cells and the chamber; and within the enclosure formed by melt, crucible, and lid inside the cell.

- Among components

Any two subunits interface as two parallel planes; because all radiation leaving one surface is incident on the other, the cumulative heat exchange of subunit i with its neighboring subunits is (see Eq. 13.24 in Incropera and DeWitt[14])

$$\dot{Q}_i^{\mathrm{rad},\parallel} = \sum_j \frac{A_{ij} \sigma (T_i^4 - T_j^4)}{\dfrac{1}{\varepsilon_i} + \dfrac{1}{\varepsilon_j} - 1} \tag{34}$$

where ε_i and ε_j are the emissivities of the two surfaces and σ is the Stefan–Boltzmann constant.

- Between cells and chamber

Radiation exchange of lid, crucible, and crucible support with the chamber is restricted by the radiation shield. The radiation shield's complicated sandwich structure is approximated as a single radiation shield with an effective emissivity $\varepsilon_{\mathrm{SH}}$ (see Eq. 13.28 in Incropera and DeWitt[14]) as follows

$$\dot{Q}_i^{\mathrm{rad,shld}} = \frac{A \sigma (T_i^4 - T_{\mathrm{chamb}}^4)}{\dfrac{1}{\varepsilon_i} + \dfrac{2 - \varepsilon_{\mathrm{SH}}}{\varepsilon_{\mathrm{SH}}}} \tag{35}$$

Then, $\varepsilon_{\mathrm{SH}}$ is an unknown model parameter that will be estimated below. Because of its size in comparison to the effusion cell, the chamber is assumed to be a black body. The temperature T_{chamb} of its water-cooled walls is assumed to be constant.

In addition, there is noninsulated direct exchange between

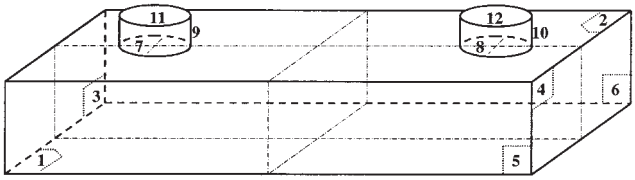

Figure 5. Nomenclature of heat exchange areas *m*.

the nozzles, that is, the lid (subunit 3) and the chamber, given by

$$\dot{Q}_3^{\text{rad,dir}} = 2\sigma\varepsilon_3 A_{\text{nozz}}(T_3^4 - T_{\text{chamb}}^4) \tag{36}$$

where A_{nozz} is the entire nozzle cross section consisting of wall and opening. This is justified because most of the radiation leaving the nozzle stems from its inside surface, not the melt (see *View Factors*).

- Within cell's enclosure

The net radiative heat flow leaving surface m within the enclosure (see Figure 5) is given by (see Eq. 13.19 in Incropera and DeWitt[14])

$$\dot{Q}_m^{\text{rad,encl}} = \frac{\sigma\mathcal{T}_m^4 - J_m}{R_m^S} \tag{37}$$

where $\mathcal{T}_m$ is the absolute surface temperature, $R_m^S = (1 - \varepsilon_m)/(\varepsilon_m A_m)$ is the surface radiative resistance, and J_m is the radiosity, that is, the radiation leaving the surface m resulting from emission and reflection (see p. 645 in Incropera and DeWitt[14]).

For melt ($i = 1$) and lid ($i = 3$), the heat flows are directly given by the heat flows from their corresponding surfaces. The crucible ($i = 2$) has four surfaces ($m = 3, \ldots, 6$) in the enclosure. Its heat flow is given by the sum of the net radiation from these surfaces.

Radiosities. To determine the radiosity, the radiation exchange arising from reflection and emission among the surfaces needs to be considered. In an N-surface enclosure, the radiosities J_m are related by a set of N equations (see Eq. 13.21 in Incropera and DeWitt[14]), as follows

$$\frac{E_{b,m} - J_m}{R_m^S} = \sum_{\substack{n=1 \\ n\neq m}}^{N} \frac{J_m - J_n}{R_{m,n}^G} \tag{38}$$

where $E_{b,m} = \sigma T_m^4$ is the black-body radiation and $R_{m,n}^G \equiv (A_m F_{m,n})^{-1}$ is a geometrical resistance. It depends on the view factor $F_{m,n}$, which is a fractional measure for the radiation leaving surface A_m that is incident on surface A_n (see *View Factors*).

Equation 38 can be rewritten as

$$\frac{R_m^S}{R_m^{GS}} J_m - \sum_{\substack{n=1 \\ n\neq m}}^{N} \frac{R_m^S}{R_{m,n}^G} J_n = E_{b,m} = \sigma\mathcal{T}_m^4 \tag{39}$$

where

$$\frac{1}{R_m^{GS}} \equiv \frac{1}{R_m^S} + \sum_{\substack{n=1 \\ n\neq m}}^{N} \frac{1}{R_{m,n}^G} \tag{40}$$

is a combined surface and geometric resistance.

Now it becomes apparent (see p. 734 in Incropera and DeWitt[14]) that this set of equations can be formulated as an easily solved system of linear algebraic equations

$$\mathbf{R} \cdot J = c \tag{41}$$

where the elements of the $N \times N$ matrix $\mathbf{R}$ depend on the surface and geometric resistances as seen on the left-hand side of Eq. 39, $J = (J_1, \ldots, J_N)^T$ and $c = \sigma(\mathcal{T}_1^4, \ldots, \mathcal{T}_N^4)^T$.

View Factors. An N-surface enclosure has N^2 view factors associated with it. Computation of all 144 view factors for the 12-surface enclosure depicted in Figure 5 would be very complicated because of its nontrivial geometry. However, evaluation of the nozzle view factor allows for a significant simplification of the problem.

Because the view factor $F_{7,9}$ is 93% (see Appendix D in Modest[19]), most radiation from within the enclosure through the nozzle is incident on the inside of the nozzle. Given that $T_9 \approx T_2$, radiation exchange through the nozzle is essentially identical to radiation exchange with the lid at T_2.

The nozzle surfaces 7–12 can then be neglected, such that only the view factors within a rectangular box ($N = 6$) need to be computed. The necessary view factors for exchange between parallel and orthogonal planes can be found in the open literature (see Appendix D in Modest[19]). Because the enclosure's geometry depends on the melt level, the view factors are a function of time. For fast on-line computation, they are generated off-line and stored in a look-up table.

Cumulative Heat Flows. After discussing the various heat transfer terms, they need to be assembled according to the geometry to determine the heat flow vector $\dot{Q}_i$ in Eq. 30. Each component i (see Figure 2) exchanges heat by conduction $\dot{Q}_i^{\text{cond}}$ (see Eq. 32) and radiation $\dot{Q}_i^{\text{rad},\|}$ (see Eq. 34) with its neighboring components. Furthermore, outside surfaces exchange radiation with the chamber through the shield $\dot{Q}_i^{\text{rad,shld}}$ (see Eq. 35) and directly by the nozzles $\dot{Q}_i^{\text{rad,encl}}$ (see Eq. 36). Subunits that form the cell's enclosure exchange radiation $\dot{Q}_i^{\text{rad,encl}}$ according to Eq. 37. Finally, melt and crucible exchange heat $\dot{Q}_{12}^{\text{conv}}$ according to Eq. 33.

For components 1–6, the cumulative heat flows are then given by

Table 2. Heat of Vaporization and $\ln(p_\infty^{\mathrm{vap}})$

Element	Range [°C]	$\Delta\hat{H}^{\mathrm{vap}}$ [kJ/mol]	$\ln(p_\infty^{\mathrm{vap}}/\mathrm{Pa})$
Copper	942–1622	323.7	25.5
Gallium	757–1372	263.9	24.2
Indium	670–1242	239.2	23.9

$$\dot{Q} = \begin{pmatrix} & \dot{Q}_1^{\mathrm{rad,encl}} + \dot{Q}_{12}^{\mathrm{conv}} \\ \dot{Q}_2^{\mathrm{cond}} + \dot{Q}_2^{\mathrm{rad},\parallel} + \dot{Q}_2^{\mathrm{rad,encl}} + \dot{Q}_{21}^{\mathrm{conv}} \\ \dot{Q}_3^{\mathrm{cond}} + \dot{Q}_3^{\mathrm{rad},\parallel} + \dot{Q}_3^{\mathrm{rad,encl}} + \dot{Q}_3^{\mathrm{rad,shld}} + \dot{Q}_3^{\mathrm{rad,dir}} \\ \dot{Q}_4^{\mathrm{cond}} + \dot{Q}_4^{\mathrm{rad},\parallel} \\ \dot{Q}_5^{\mathrm{cond}} + \dot{Q}_5^{\mathrm{rad},\parallel} \\ \dot{Q}_6^{\mathrm{cond}} + \dot{Q}_6^{\mathrm{rad},\parallel} + \dot{Q}_6^{\mathrm{rad,shld}} \end{pmatrix} \tag{42}$$

Thermocouple sensor model

The effusion source's temperature is measured by a type C thermocouple (TC). The harsh environment of the deposition process requires use of sheathed thermocouples. Although the sheath offers protection against failure, it also causes undesired dynamic behavior that needs to be modeled.

Assuming first-order behavior, the manufacturer provides the time constant τ_{TC} as a function of sheath diameter (see p. Z-51 in *Omega Temperature Handbook*[20]). In addition, both a gain K_{TC} of <1 and a time delay α_{TC} are observed experimentally. Because the thermocouple is inserted into the crucible (see Figure 2), its temperature T_{TC} depends on the crucible temperature T_{cruc} such that its transfer function is given by

$$M_{\mathrm{TC}} = \frac{K_{\mathrm{TC}} e^{-\alpha_{\mathrm{TC}} s}}{\tau_{\mathrm{TC}} s + 1} = \frac{\Delta T_{\mathrm{TC}}}{\Delta T_{\mathrm{cruc}}} \tag{43}$$

where ΔT_{TC} and ΔT_{cruc} are deviation variables based on the initial temperature T_0, that is,

$$\Delta T_{\mathrm{TC}} = T_{\mathrm{TC}} - T_0 \tag{44}$$

$$\Delta T_{\mathrm{cruc}} = T_{\mathrm{cruc}} - T_0 \tag{45}$$

The unknown parameters K_{TC} and α_{TC} are estimated in the next section.

Model Parameters

Two kinds of parameters are required: (1) thermodynamic, physical, and radiation property data for copper, gallium, indium, graphite, and boron-nitride; and (2) system parameters such as heater efficiency, effective effusion shield emissivity, and AA model constants.

Although the developed model is applicable to all three effusion sources, its parameter estimation and evaluation is performed only for the copper source for brevity: (1) operationally, it is the most prone to problems because of its high temperature; and (2) temperature-dependent data (heat capacity, emissivity) for copper are more easily available in the open literature.

Literature data

Vapor Pressure and Heat of Vaporization. The heat of vaporization can be obtained from vapor pressure data by means of the Clapeyron–Clausius equation (see p. 308 in Sandler[21]):

$$\frac{d\,\ln(p^{\mathrm{vap}})}{dT} = \frac{\Delta\hat{H}^{\mathrm{vap}}}{RT^2} \tag{46}$$

When defining p_∞^{vap} as the hypothetical vapor pressure at infinite temperature, integration of Eq. 46 results in

$$\ln\left(\frac{p^{\mathrm{vap}}}{p_\infty^{\mathrm{vap}}}\right) = -\frac{\Delta\hat{H}^{\mathrm{vap}}}{RT} \tag{47}$$

that is, a plot of $\ln(p^{\mathrm{vap}})$ vs. $1/T$ should give a straight line with a slope equal to $-\Delta\hat{H}^{\mathrm{vap}}/R$ if the heat of vaporization is independent of temperature for the analyzed temperature interval. For the data given by Dushman[22] (see Table 10.1 therein), least-squares parameter estimates are given in Table 2.

Physical and Thermodynamic Properties. Physical and thermodynamic properties of copper, gallium, and indium are given in Table 3. The data are as follows: molecular weight M (see pp. 1–12 in Lide[23]), normal melting (T_m) and boiling (T_b) points (see pp. 4–132 in Lide[23]), van der Waals diameter σ (see p. 257 in Pauling[24]), mass specific heats of fusion $\Delta\hat{H}^{\mathrm{fus}}$ (see pp. 6–123 in Lide[23]), and vaporization $\Delta\hat{H}^{\mathrm{vap}}$, and liquid density ρ_m at the melting point (see pp. 4–137 in Lide[23]).

Heat Capacity. Because the temperatures of the effusion cell's components change over a wide range of values (from room temperature up to 1800°C for the graphite heater), the change of heat capacity with temperature has to be taken into account. For copper, the linear relationship proposed by Eggers et al.[25] (see p. 752 therein)

$$c_p^{\mathrm{Cu}}(T) = a + bT \tag{48}$$

where c_p in J kg^{-1} K^{-1} is used. Although the relationship has an upper temperature limit of 1084°C, data from the literature (see p. 51 in Touloukian and Buyco[26]) justify extrapolation up to 1500°C.

For graphite (GR), data from Touloukian and Buyco[27] (see p. 9 therein) was used for least-squares parameter fitting of the logarithmic equation

$$c_p^{\mathrm{GR}}(\vartheta) = af(\vartheta) + b \tag{49}$$

with

Table 3. Physical and Thermodynamic Properties

Symbol	Unit	Copper	Gallium	Indium
M	g/mol	63.55	69.72	114.82
ϑ_m	°C	1084.62	29.76	156.60
ϑ_b	°C	2562.00	2204.00	2072.00
σ	Å	2.35	2.49	2.99
$\Delta\hat{H}^{\mathrm{fus}}$	kJ/kg	208.67	80.17	28.57
$\Delta\hat{H}^{\mathrm{vap}}$	kJ/kg	5093.80	3785.52	2083.18
ρ_m	g/cm^3	8.02	6.08	7.02

Table 4. Parameters for Heat Capacity Relations*

Parameter	Copper	Graphite	BN (low)	BN (high)
ϑ_{min}	25.0	50.0	25.0	1176.8
ϑ_{max}	1500.0	2500.0	1176.8	2000.0
a	3.5621×10^{2}	2.7659×10^{2}	3.8719×10^{2}	3.8509
b	9.8765×10^{-2}	1.8323×10^{3}	1.5820×10^{3}	1.9621×10^{3}
μ_1	—	6.9121	6.0632	1.5088×10^{3}
μ_2	—	7.2940×10^{-1}	1.0340	2.3271×10^{2}

*Temperatures in °C.

$$f(\vartheta) = \frac{\ln(\vartheta) - \mu_1}{\mu_2} \tag{50}$$

with ϑ in °C. Here, the $\ln(\vartheta)$ data are normalized with the mean (μ_1) and standard deviation (μ_2) to improve the numerical properties of Matlab's *polyfit* algorithm (see pp. 12–22 in *Using MATLAB*[28]).

For boron-nitrite (BN), the data in Touloukian and Buyco[27] (see p. 1078 therein) are best fitted by two separate regimes: (1) a logarithmic equation for low temperatures and (2) a linear equation for high temperatures

$$c_p^{BN,low}(\vartheta) = af(\vartheta) + b \tag{51}$$

$$c_p^{BN,high}(\vartheta) = ag(\vartheta) + b \tag{52}$$

with

$$g(\vartheta) = \frac{\vartheta - \mu_1}{\mu_2} \tag{53}$$

with $\vartheta_{switch} = 1176.8$°C as the switching point between the two regimes.

The parameter values are summarized in Table 4. Also given are the minimum (ϑ_{min}) and maximum (ϑ_{max}) temperatures of validity for the corresponding relationship. For lower or higher temperatures, the corresponding heat capacities at ϑ_{min} and ϑ_{max} are used instead.

Emissivity. For the emissivity of molten copper, *Perry's Chemical Engineers' Handbook*[29] (see Tables 5 and 6 therein) gives the following linear relationship

$$\varepsilon^{Cu}(T) = \varepsilon_1 + \frac{T - T_1}{T_2 - T_1}(\varepsilon_2 - \varepsilon_1) \tag{54}$$

with $T_1 = 1349.8$ K, $T_2 = 1549.8$ K, $\varepsilon_1 = 0.16$, and $\varepsilon_2 = 0.13$.

For graphite, only values of the absorptivity α are reported as a function of temperature in the literature (see pp. 5–26 in Perry[29] and pp. 15–24 in Rohsenow and Hartnett[30]). For gray surfaces, as assumed above, it is equal to the emissivity (see p. 674 in Incropera and DeWitt[14]). This is confirmed by the data given by Pierson[31] (see p. 109 therein). Least-squares parameter fitting of

$$\varepsilon^{GR}(\vartheta) = af^3(\vartheta) + bf^2(\vartheta) + cf(\vartheta) + d \tag{55}$$

gives $a = -1.3797 \times 10^{-2}$, $b = 5.6707 \times 10^{-4}$, $c = 1.1048 \times 10^{-1}$, $d = 7.1334 \times 10^{-1}$, $\mu_1 = 7.1835$, and $\mu_2 = 9.6716 \times 10^{-1}$.

Table 5. Thermal Conductivity k in W m^{-1} K^{-1} at Typical Operating Point ϑ in °C

Variable	Cu	Ga	In	GR-Lo	Gr-Hi	BN
ϑ	1380	1060	1000	1250	1800	1000–1650
k	175.5	133.9	75.3	43	39	23

Thermal Conductivity. Thermal conductivities are required to estimate the Biot number. The values are given at a typical operating point for each subunit (see Table 5).

For copper (see p. 81 in Touloukian et al.[32]), the values vary by <9% from ϑ_m to 1600°C. For gallium and indium (see pp. 107 and 151, respectively, in Touloukian et al.[32]), the values had to be extrapolated from literature data. For graphite (see Figure 11.2 in Sheppard et al.[33]), two values are given because the temperatures of crucible support ($\vartheta_{Lo} \approx 1250$°C) and heater ($\vartheta_{Hi} \approx 1800$°C) are very different. For boron-nitride (see p. 656 in Touloukian et al.[34]), k is approximately constant between 1000 and 1650°C.

Estimated data

The goal of this section is to estimate the remaining parameters. This is done for the desired operating points based on specific identification experiments. As before, the analysis is limited to the copper source.

Overview of Parameters and Constraints. Table 6 gives an overview of the 10 unknown model parameters including bounds, reasonable range for parameter estimation, and initial guesses. The parameters stem from three parts of the model, that is, two from the thermocouple model, six from the heat transfer model, and two from the atomic absorption model.

The occurrence of m_0 in the list of parameters requires an explanation. Although this initial mass need not be unknown, it generally is because it is cumbersome to measure. On the other hand, it is easily estimated by the time it takes the material to solidify (see below).

The estimate for the boron-nitride emissivity is taken from Tucker and Meyer[35] (see Table III therein). For the AA model, the estimates of κ and γ are taken from Hanket[13] (see p. 360 therein) and Junker et al.[4] (see Eq. 10 therein), respectively.

Integration of the Process Model. Mass and heat transfer models form a set of nine coupled nonlinear ordinary differential equations. It is implemented and integrated in Matlab using the third-order Adams–Bashforth method ODE113. Proper initialization of the ODE solver requires all simulations to start at room temperature where all model states are known.

Computational cost is reduced by interpolating both the vapor flow rate and the view factors from a precomputed

Table 6. Unknown Model Parameters $\mathcal{P}$ with Units, Grouped by Model Membership (Thermocouple, Heat Transfer, and Atomic Absorption), Description, Equation of First Occurrence, Full Range R_F, Reasonable Range R_R, and Initial Guess $\mathcal{P}_0$

$\mathcal{P}$	Unit	Description	Eq.	R_F	R_R	$\mathcal{P}_0$
K_{TC}	–	TC model gain	43	[0, 1]	[0.8, 1.0]	1.0
α_{TC}	s	TC model time delay	43	[0, ∞)	[0, 60]	0
ε_{BN}	–	Emissivity of boron-nitride	34	[0, 1]	[0.01, 0.3]	0.18
ε_{SH}	–	Effective emissivity of radiation shield	35	[0, 1]	[0.01, 0.3]	0.1
C_{ij}	W m^{-2} K^{-1}	Contact conductance	32	[0, ∞)	[0, 2000]	150
U_{12}	W m^{-2} K^{-1}	Heat transfer coefficient	33	[0, ∞)	[0, 5000]	1500
m_0	g	Initial melt mass	1	[0, 300]	[50, 250]	150
η_{el}	–	Efficiency of electric heater	31	[0, 1]	[0.8, 1.0]	1.0
κ	m^2/kg	AA model mass extinction coefficient	27	[0, ∞)	[10^8, 10^{10}]	1.1×10^9
γ	1/m	AA model path integral	27	[0, ∞)	[0.5, 3.0]	0.42

look-up table. The average execution time is very short. On a 1.7-GHz mobile Pentium-IV PC with 640 MB RAM, running Microsoft® Windows® XP Professional and MATLAB (Version 6.5, Release 13), it takes about 35 s to simulate a 3-h experiment.

Data for Parameter Estimation. For controller design, accurate prediction of the absolute temperature and its dynamic behavior is needed for high temperatures because this is the region of normal process operation. For identification, three experiments at different operating points were performed (see Table 7 and Figures 6–8).

For each experiment, the process is first driven to and then held at the operating point for about 20 min. Then, using a relay controller at different input levels, each group of three sets of experiments is performed for another 20 min each to set the process in sustained oscillations of varying amplitude. The frequency of oscillation is the process's ultimate period.[36]

The atomic absorption measurements are very noisy and have to be filtered before being useful for parameter estimation. A third-order lowpass Butterworth filter with a normalized cutoff frequency of $W_n = 0.05$ and a sampling time of 2 s is designed and applied forward and backward to achieve zero-phase filtering (that is, filtering without a phase shift). This is accomplished by the *butter* and *filtfilt* commands, respectively, from Matlab's Signal Processing Toolbox.[37] The filter's effectiveness is demonstrated in Figure 9. The temperature measurements are filtered as well; however, with $W_n = 0.15$, a weaker filter with a higher cutoff frequency is used.

The atomic absorption measurements are not only very noisy but also exhibit a strong baseline drift, which can be seen in Figures 7 and 8 from the fact that the absorbance drops from an initial value of zero to −20% after the run. The most likely cause for this is deposition of material on the optics and insufficient compensation by the measurement unit. This baseline drift makes it difficult to properly estimate the AA model's unknown parameters.

Objective Function and Solution Strategy. The primary criterion for fitting the model parameters is to match the absolute values and the dynamics of both temperature and absorbance measurements while the process is operating in the high temperature region (that is, at its setpoint). The residuals are defined as

$$e_k(\vartheta_{TC}) = \vartheta_{exp,k} - \vartheta_{TC,k} \tag{56}$$

where k is the current sampling index, $\vartheta_{exp,k}$ is the measured temperature, and $\vartheta_{TC,k}$ is the simulated thermocouple measurement. For the absorbance, the residual $e_k(\alpha)$ is defined likewise.

The goodness-of-fit is then checked by the root-mean-square (RMS) error

$$\mathrm{RMS}_{TC} = \left[\frac{1}{k_2 - k_1}\sum_{k=k_1}^{k_2} e_k^2(\vartheta_{TC})\right]^{0.5} \tag{57}$$

where k_1 and k_2 denote the beginning and end of the high temperature region, respectively.

Minimization of RMS_{TC} by a simultaneous estimation of the 10 unknown model parameters is not practical. Instead, the way the experimental system's compartments are interconnected allows for a sequential technique that requires a simultaneous estimation of only four parameters (see below). For instance, K_{TC} can be estimated independently from all other parameters, but estimation of the heat transfer model parameters is not possible without knowledge of K_{TC}. Likewise, estimation of $\kappa\gamma$ requires proper temperature predictions from the heat transfer model, but prediction of the temperature does not require knowledge of $\kappa\gamma$. This technique requires some degree of iteration but is much faster than a direct simultaneous approach.

Thermocouple Sensor Model

- Gain K_{TC}

The gain can be estimated directly from the experiments by observing that the measured phase transition does not occur at the melting point of copper ($\vartheta_m = 1084.62$°C) but at a much

Table 7. Estimates for Heat Transfer Model Parameters, Relative Error in Prediction of the Measured Temperature, and Estimated Error in Prediction of the Flow Rate

Run	ϑ_d [°C]	m_0 [g]	U_{12} [W m^{-2} K^{-1}]	C_c [W m^{-2} K^{-1}]	ε_{BN}	ε_{SH}	RMS_{TC} [°C]	MN_{TC} [°C]	AMN_{TC} [°C]	E_{TC} [%]	$\bar{\vartheta}^{est}_{melt}$ [°C]	$\mathrm{AMN}^{est}_{cruc}$ [°C]	$\overline{\Delta\vartheta}^{est}_{melt,cruc}$ [°C]	$\mathrm{AMN}^{est}_{melt}$ [°C]	$E^{est}_{\dot{m}_{vap}}$ [%]
1	1170	200	1500	150	0.125	0.16	7.91	2.33	5.59	0.48	1280.7	6.14	1.47	7.61	13
2	1210	200	1500	150	0.1	0.16	5.98	0.62	4.66	0.39	1325.7	5.12	1.67	6.79	11
3	1260	200	1500	150	0.09	0.16	7.77	0.59	6.47	0.51	1379.9	7.11	1.85	8.96	13

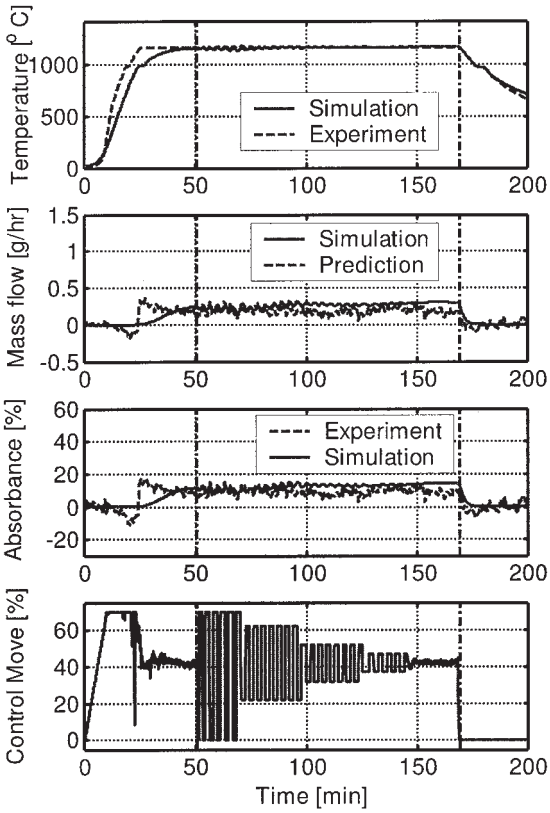

Figure 6. Parameter estimation experiment #1.

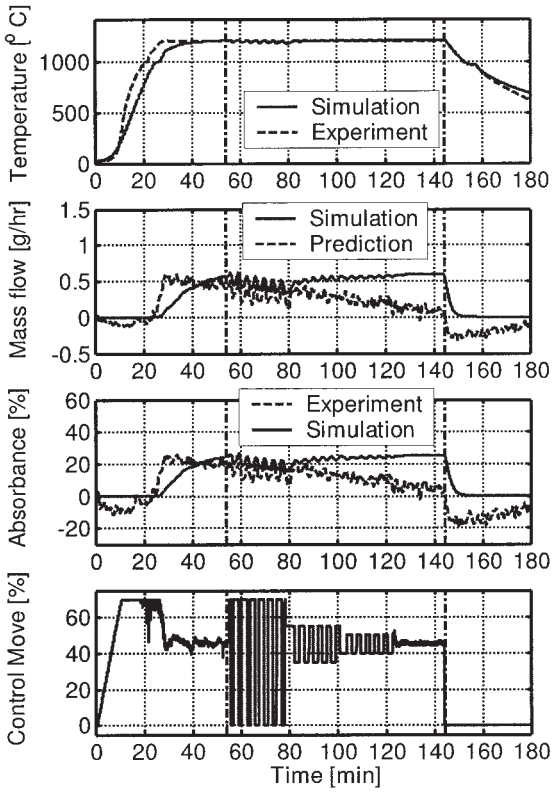

Figure 7. Parameter estimation experiment #2.

lower temperature of approximately $\vartheta_{m,\mathrm{exp}} = 990°\mathrm{C}$. Assuming K_{TC} is constant, it is given by the ratio of the actual and the measured melting temperatures. For an initial temperature of $\vartheta_0 = 30°\mathrm{C}$, the gain is thus given by

$$K_{\mathrm{TC}} = \frac{\Delta\vartheta_{m,\mathrm{exp}}}{\Delta\vartheta_m} = \frac{(990 - 30)°\mathrm{C}}{(1084.62 - 30)°\mathrm{C}} = 0.91 \qquad (58)$$

The fact that the required gain is <1 indicates that heat is conducted away from the crucible such that the measured temperature is less than the actual temperature. Therefore, the assumption that the thermocouple does not influence the crucible is not entirely correct. Along with the other assumptions, it is justified a posteriori because the heat-transfer model is capable of correctly predicting the experimentally observed behavior (see Model Evaluation).

- Time delay α_{TC}

The time delay cannot be estimated unless a good prediction from the heat transfer model has been obtained. Because the thermocouple model does not influence any other model equation, this value can safely be assumed to be zero initially. Once a good temperature prediction is available, the time delay is estimated by comparing the phase of the relay induced oscillations of measurement and prediction. This method is preferred to a simple step test because it is easier to evaluate. This way, a time delay of

$$\alpha_{\mathrm{TC}} = 25\ \mathrm{s} \qquad (59)$$

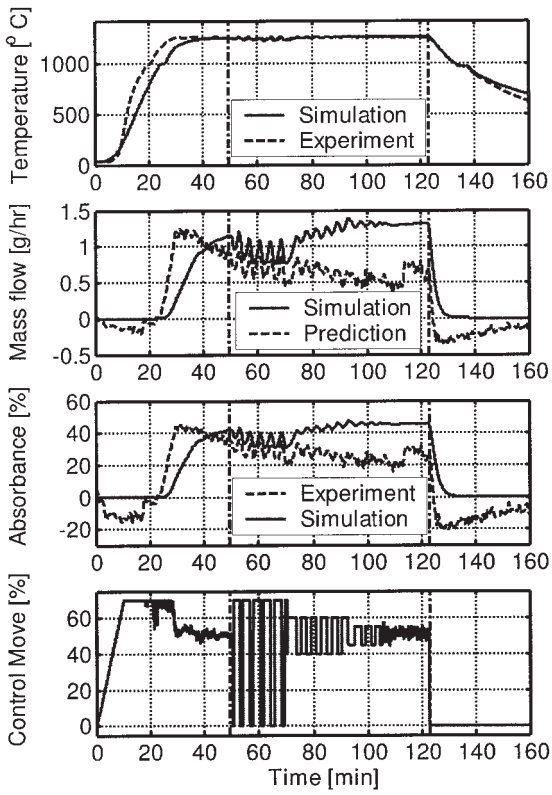

Figure 8. Parameter estimation experiment #3.

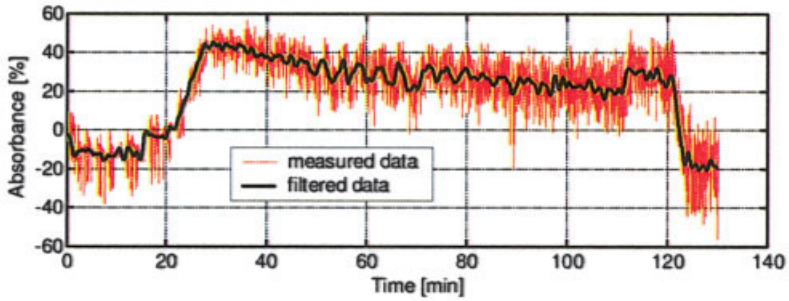

Figure 9. Noise filtering for atomic absorption measurements for the experiment at T_d = 1260°C.

[Color figure can be viewed in the online issue, which is available at www.interscience.wiley.com]

has been estimated. This value yields good predictions of the phase for all three experiments (see Figure 10).

Heat-Transfer Model

- Efficiency η_{el}

Because conduction within subunits has been neglected, the model does not perform well in predicting the start-up from room temperature. By assuming a heater efficiency of

$$\eta_{el} = 1 \tag{60}$$

the fastest heat-up, and thus the smallest error between measurement and prediction, can be guaranteed.

- Contact conductances C_{ij}

Estimation of contact conductances is simplified by assuming that the conductances for the two different interfaces, that is, graphite/boron-nitride and boron-nitride/boron-nitride, do not differ much, that is,

$$C_{ij} = C_c = \text{const.} \tag{61}$$

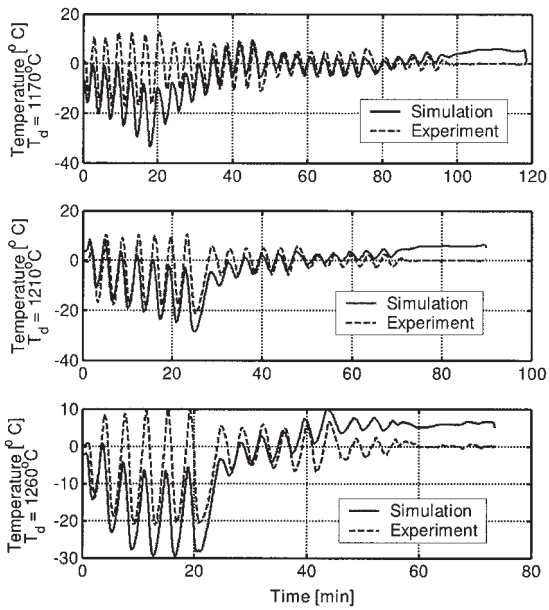

Figure 10. Close-up of deviation from the T_d = [1170, 1210, 1260]°C setpoint for parameter estimation experiments.

This is justified a posteriori because the solution does not depend strongly on C_c.

- Initial mass m_0

Although the entire model's dynamic behavior depends on the melt mass, this becomes most apparent during melting and solidification at start-up and shutdown, respectively. In these phases, there is a characteristic saddle point in the temperature profiles (see Figures 6–8).

Assuming a constant heat flow $\dot{Q}_1 > 0$ from the melt during cool down, the length of the phase transition is directly proportional to the initial melt mass. A straightforward integration of Eq. 1 using the initial condition $m_s(t = 0) = 0$ results in

$$m_s(t) = \frac{\dot{Q}_1}{\Delta \hat{H}^{fus}} t \tag{62}$$

Because the parameter estimation experiments are short ($t \approx$ 2.5 h), the change of melt mass ($\Delta m \approx 1.5$ g) can be neglected. Then, the time t_s needed for complete solidification is

$$t_s = \frac{m_s(t_s)}{\dot{Q}_1/\Delta \hat{H}^{fus}} \approx \frac{m_0}{\dot{Q}_1/\Delta \hat{H}^{fus}} \tag{63}$$

The assumption of constant melt mass would not be necessary when performing the parameter fit during start-up. However, because the heat transfer model does not predict the heat-up phase very well, this would not allow for an accurate estimation of m_0.

Strategy for Remaining Parameters. After eliminating η_{el}, reducing the estimation of contact conductances to C_c, and discussing the estimation of m_0, the remaining five parameters are identified by a two-step iteration. The four parameters characteristic for the heat exchange are combined into the parameter vector $\mathcal{P}_{HX}$, that is,

$$\mathcal{P}_{HX} \equiv [U_{12}, C_c, \varepsilon_{BN}, \varepsilon_{SH}] \tag{64}$$

The iteration then proceeds as follows:

(1) Based on the current estimate of $\mathcal{P}_{HX}$, predict the temperature profiles and estimate m_0 such that the simulated phase change from liquid to solid takes equally long as in the experiment.

(2) Based on this value of m_0, estimate the parameters $\mathcal{P}_{HX}$ to reduce RMS_{TC}.

(3) Stop, if desired RMS_{TC} is achieved; otherwise, go back to step 1.

In this algorithm, step 1 converges very quickly, whereas step 2 takes the most effort. In other words, the overall prediction is not very sensitive to the initial mass, which is why this sequential approach works well. Estimation of $\mathcal{P}_{HX}$ is discussed next.

- Parameters $\mathcal{P}_{HX}$

Based on the initial guess values in Table 6, estimates for these parameters were improved by (1) an optimized step-size random search (OSSRS) method[38] and (2) a sensitivity study. In addition to RMS_{TC}, the parameter fits are compared regarding their:

(1) Mean error MN_{TC}

$$MN_{TC} = \frac{1}{k_2 - k_1} \sum_{k=k_1}^{k_2} e_k(\vartheta_{TC}) \tag{65}$$

which gives an indication of relative location of the predicted and experimental temperature profiles. It is negative if the simulated profiles are entirely larger than the experimental profiles, positive if they are entirely smaller, and close to zero, otherwise.

(2) Absolute mean error AMN_{TC}

$$AMN_{TC} = \frac{1}{k_2 - k_1} \sum_{k=k_1}^{k_2} |e_k(\vartheta_{TC})| \tag{66}$$

which gives the best indication of the actual prediction error. Unlike RMS_{TC}, large errors are weighed the same way as small errors, and unlike MN_{TC}, positive and negative errors cannot cancel.

(3) Relative error E_{TC} in predicting the temperature

$$E_{TC} = 100 \cdot \frac{AMN(\vartheta_{TC})}{\vartheta_d} \tag{67}$$

More important than E_{TC} is the relative error in flow rate prediction $E_{\dot{m}_{vap}}$ because the ultimate goal of this model is to properly predict the flow rate for process control of the deposition process. Its computation is not straightforward because neither the experimental melt temperature nor the error in its prediction is known. To estimate this value, four quantities are needed:

(1) The mean of the simulated melt temperature $\bar{\vartheta}^{est}_{melt}$, which is estimated by

$$\bar{\vartheta}^{est}_{melt} = \frac{1}{k_2 - k_1} \sum_{k=k_1}^{k_2} \vartheta_{melt,k} \tag{68}$$

(2) The absolute mean error AMN^{est}_{cruc} in predicting the crucible temperature, which is estimated from the absolute mean error AMN_{TC} and the gain of the thermocouple model K_{TC} as

$$AMN^{est}_{cruc} = \frac{AMN(\vartheta_{TC})}{K_{TC}} \tag{69}$$

(3) The mean of the difference in simulated melt and crucible temperature $\overline{\Delta\vartheta}^{est}_{melt,cruc}$, which is estimated by

$$\overline{\Delta\vartheta}^{est}_{melt,cruc} = \frac{1}{k_2 - k_1} \sum_{k=k_1}^{k_2} (\vartheta_{melt,k} - \vartheta_{cruc,k}) \tag{70}$$

(4) The absolute mean error AMN^{est}_{melt} in predicting the melt temperature, which is estimated by a sum of the previous two quantities

$$AMN^{est}_{melt} = AMN^{est}_{cruc} + \overline{\Delta\vartheta}^{est}_{melt,cruc} \tag{71}$$

The relative error $E_{\dot{m}_{vap}}$ in flow rate prediction is then computed by the flow model according to

$$E^{est}_{\dot{m}_{vap}} = 100 \cdot \frac{\dot{m}_{vap}(\bar{\vartheta}^{est}_{melt} + AMN^{est}_{melt}) - \dot{m}_{vap}(\bar{\vartheta}^{est}_{melt})}{\dot{m}_{vap}(\bar{\vartheta}^{est}_{melt})} \tag{72}$$

where the dependency of the flow rate on the melt temperature is shown in Figure 3.

The estimated parameters along with error measures for both temperature and flow rate prediction for the estimation experiments are summarized in Table 7. MN_{TC} is much smaller than AMN_{TC}, which indicates that the simulated temperature profiles are both above and below the experimental profiles (see Figures 6–8).

E_{TC} is much smaller than $E_{\dot{m}_{vap}}$, which is consistent with intuition, given that the flow rate depends exponentially on the temperature. With less than 13% on average, the model's prediction is still accurate enough for model-based deposition control (see Junker et al.[4]).

- Sensitivity study

This section discusses the sensitivity study of estimation run #1 for the parameters given in Table 7. The purpose is to give some insights on the optimal value's dependency on each pair of parameters for the six possible combinations (see Figure 11).

Two kinds of dependencies occur: the lowest RMS has (1) a hyperbolic ridge shape for all three combinations of ε_{BN}, ε_{SH}, and C_c (top left, middle left, and right); and (2) a linear ridge shape for all three combinations involving U_{12} (top right, bottom left, and right).

Clearly then, assuming that the observed behavior is also true for small variations of $\mathcal{P}_{HX}$, U_{12} has no strong influence on the optimal value. Consistency of this hypothesis was cross-checked in a separate sensitivity study varying only one of the four parameters at a time (see Figure 2.16 in Junker[39]). That study shows also that the effect of C_c is negligible compared to that of ε_{BN} and ε_{SH}, which is consistent with Figure 11.

An analysis of the contour plots reveals that the current RMS is very close to the optimum for every single binary combination. However, because only binary dependencies are analyzed, possible interactions might be missed, and there is the possibility for improvement of the fit.

Atomic Absorption Sensor Model. The AA sensor model has two unknown parameters that appear only as the product $\kappa\gamma$, which results in an identifiability problem, and only the value of this product can be determined. Estimation of this combined parameter depends on the mass and heat transfer

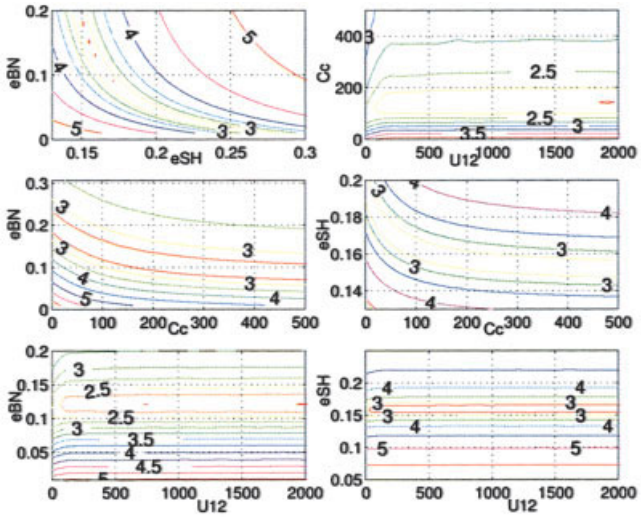

Figure 11. Sensitivity study contour plots of estimation of experiment #1.

Legend: *z*-axis [ln(RMS/°C)], boron-nitride emissivity "e_{BN}", radiation shield emissivity "e_{SH}" [–], heat transfer coefficient between melt and crucible "U_{12}" [W m^{-2} K^{-1}], and contact conductance "C_c" [W m^{-2} K^{-1}].

[Color figure can be viewed in the online issue, which is available at www.interscience.wiley.com]

models because the absorption depends on the vapor flow rate, which, in turn, depends on the melt temperature.

Because the AA measurements are fraught with strong baseline drift (see Figure 9), an estimation by a sum-squared error is of little use. The signal is, however, approximately constant during the first 5–10 min after reaching the temperature setpoint, such that $\kappa\gamma$ can be determined during this early stage of each experiment. For all three experiments, a good prediction is achieved for

$$\kappa\gamma = 16.0 \times 10^8 \text{ m/kg} \tag{73}$$

Results. In this section, the obtained results are compared graphically by plotting both the experimental and the simulated data in a single plot for each parameter estimation experiment (see Figures 6–8). The plots show from top to bottom: (1) simulated and measured TC temperatures, (2) simulated mass flow and mass flow predicted from absorbance measurements by the absorbance model, (3) simulated and measured absorbance, and (4) control moves. The dash–dotted vertical lines indicate the region of the parameter fit. As expected from the discussion in the previous sections, the results are very good for all three experiments. Based on the available absorbance data, even this prediction is reasonably good. To assess the accuracy of the absorbance model better, better measurements would be required.

The mass flow rates and absorbances of experiments #2 and #3 exhibit an opposite trend toward the end of the experiment. The decrease in the experimental measurements is caused by sensor drift. The increase in model predictions is caused by a corresponding drift in the TC temperature prediction. Because the mean value of the measured temperature is constant, neither the upward nor the downward drift is physical. Sensor drift is also the reason for the measured absorbance to drop below zero after the experiment.

A close-up of the relay controller induced oscillations (see Figure 10) shows that the model accurately predicts phase and frequency of these oscillations. After detrending the results, the amplitude prediction is off by a factor of about 1.25.

The prediction is least accurate with respect to the trends. Because the mean process output is held constant by the relay controller, there should be no trend in the prediction either. Its presence hints at an imbalance in the emissivities of radiation shield and boron-nitride, effectively resulting in too much heat loss at the beginning and too little heat loss at the end of the analyzed interval.

Model Evaluation

In this section, the model's ability to predict both temperature and absorbance profiles is crosschecked in two independent experiments. In addition, consistency of the lumped capacitance assumption is checked by computing the Biot number.

Temperature and absorbance

For evaluation of the temperature prediction, the same analyses as those for the parameter estimation are performed. The results for temperature and flow rate prediction are summarized in Table 8.

During the evaluation experiment, the thermocouple's behavior was different from the behavior during the estimation experiments. The phase transition during heat-up was not at 990°C but at 965°C. To compensate for this, the setpoint was reduced to $T_d = 1230$°C (see Figure 12). This different behavior is also proved by an absorbance of 70% at $T_d = 1260$°C. After reducing the setpoint, it decreased to 45% again, as expected.

For proper evaluation of this experiment, the thermocouple gain K_{TC} was thus reestimated based on Eq. 58, as follows:

$$K_{TC,new} = \frac{\Delta\vartheta_{m,exp}}{\Delta\vartheta_m} = \frac{(965 - 27.8)°C}{(1084.62 - 27.8)°C} = 0.89 \tag{74}$$

Table 8. Temperature and Flow Rate Prediction Errors for Evaluation Experiment #1

Run	ϑ_d [°C]	ε_{BN}	RMS_{TC} [°C]	MN_{TC} [°C]	AMN_{TC} [°C]	E_{TC} [%]	$\bar{\vartheta}^{est}_{melt}$ [°C]	AMN^{est}_{cruc} [°C]	$\overline{\Delta\vartheta}^{est}_{melt,cruc}$ [°C]	AMN^{est}_{melt} [°C]	$E^{est}_{\dot{m}_{vap}}$ [%]
New K_{TC}	1230	0.09	8.71	5.16	5.70	0.46	1377.1	6.42	1.86	8.28	12
Old K_{TC}	1230	0.09	27.73	−26.76	26.76	2.18	1377.2	29.39	1.86	31.25	54
Lower ε_{BN}	1230	0.085	7.23	1.53	5.60	0.46	1381.2	6.32	1.88	8.20	12
Higher ε_{BN}	1230	0.095	11.00	8.47	8.47	0.69	1373.4	9.56	1.83	11.39	17

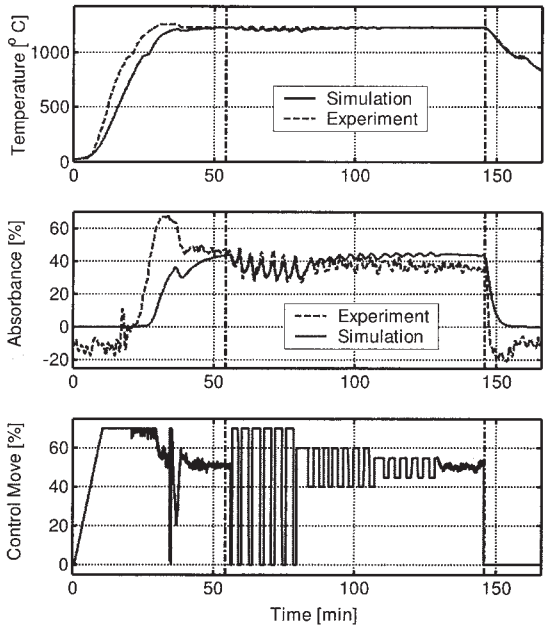

Figure 12. Evaluation experiment #1.

where a different initial temperature of $\vartheta_0 = 27.8°C$ was also taken into account.

The obtained simulation results are shown in Figures 12 and 13. During the first set of oscillations (0–30 min), there appears to be a transient in the model because the mean value first decreases and then levels off. The same can be seen in the second set (30–60 min). A possible reason is a not properly assessed temperature dependency of the emissivities because the model is very sensitive to even small variations in these parameters (see Figure 13). The obtained results are essentially identical to those obtained for the $T_d = 1260°C$ parameter estimation experiment (see Table 7). Therefore, this evaluation experiment successfully demonstrates the model's consistency for this setpoint.

To further illustrate the goodness-of-fit, it was compared to the one obtained when using the original thermocouple gain. These results are clearly much worse, thus justifying reestimation of the TC gain. Simulation of the evaluation experiment was repeated for a slight variation of $\varepsilon_{BN} = 0.08 \pm 0.005$ to verify whether better predictions are possible. The estimation based on $\varepsilon_{BN} = 0.085$ is indeed better than the estimation based on the fitted parameters. Although this indicates that better parameter values do exist, it does not invalidate the estimated parameters. The fact that both RMS_{TC} and MN_{TC} are smaller, but that AMN_{TC} is almost identical, indicates that the prediction for $\varepsilon_{BN} = 0.085$ is more centered around the experimental data (see Figure 13).

Figure 14 shows the results of a reference tracking experiment at $T_d = 1144°C$. Because of the change in the TC gain, it corresponds to the $T_d = 1170°C$ setpoint of the parameter estimation experiments. With $T_d = [1170, 1210, 1260]°C$, model parameters were estimated for a range of temperatures. The evaluation experiment discussed above is consistent with the estimation experiments for the upper end of this range. For this experiment, an RMS of 3.41°C is achieved, which shows consistency of the process model for the lower end of this temperature range.

Biot number

To check the Biot number, three pieces of information are needed: (1) the thermal conductivity, (2) a characteristic length, and (3) the external heat transfer coefficient. Thermal conductivity as a function of temperature is available in the literature (see Table 5). For the characteristic length, the largest thickness of each subunit is used to obtain a conservative estimate. Estimation of the heat transfer coefficient according to Eq. 29 is not straightforward because every subunit i of the effusion source is subject to multiple heat fluxes that occur at different interfaces with different temperature gradients from its neighboring subunits j. The value is thus estimated by summation of the individual heat transfer contributions, that is,

$$h_i^{\text{eff}} = \sum_j h_{i,j}^{\text{eff}} = \sum_j \frac{\dot{Q}_{i,j}}{A_i(T_i - T_j)} \tag{75}$$

where the individual heat flows $\dot{Q}_{i,j}$ are given in Eq. 42.

To describe the contribution of radiation within the enclosure, Eq. 37 cannot be used because it describes the cumulative heat flows leaving subunits 1–3. Because these subunits have different temperatures, the *individual* fluxes ($\dot{q} = \dot{Q}/A$) *between* these units (that is, $\dot{q}_{1,2}^{\text{rad,encl}}$, $\dot{q}_{1,3}^{\text{rad,encl}}$, $\dot{q}_{3,2}^{\text{rad,encl}}$) are needed. They are computed by

$$\dot{q}_{i,j}^{\text{rad,encl}} = \sum_n F_{m,n}(J_m - J_n) \tag{76}$$

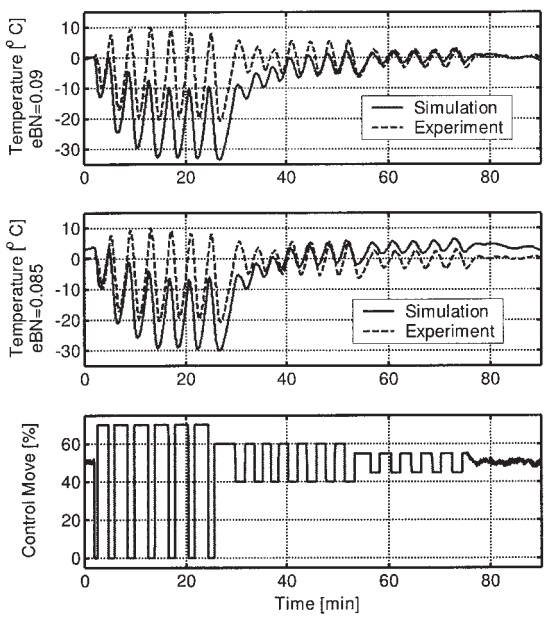

Figure 13. Close-up of deviation from the $T_d = 1230°C$ setpoint for evaluation experiment #1 for two different boron-nitride emissivities.

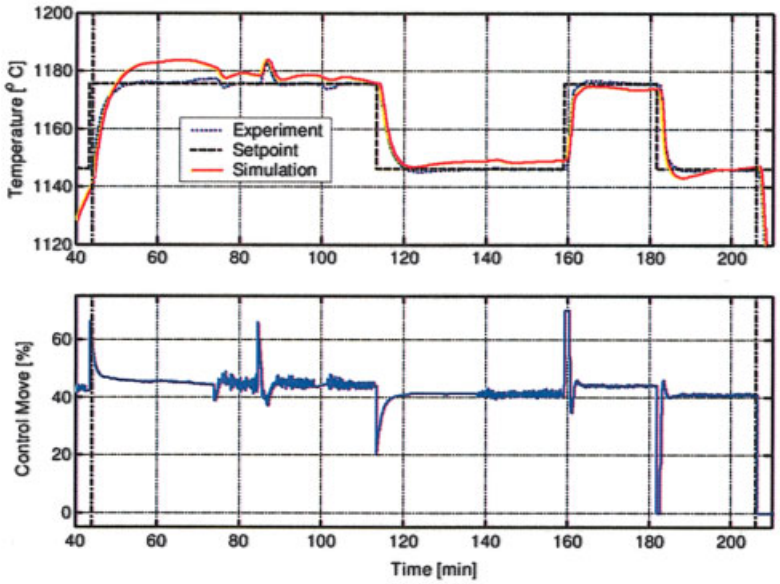

Figure 14. Close-up of temperature prediction for evaluation experiment #2.

[Color figure can be viewed in the online issue, which is available at www.interscience.wiley.com]

which follows directly from equating Eqs. 37 and 38. Here, m is the heat exchange surface corresponding to subunit i, and n are the heat exchange surfaces corresponding to subunit j.

The obtained results for evaluation experiment #1 are shown in Figure 15. For all subunits but melt and crucible, the estimated Biot number is <0.1 throughout the entire experiment. The values for melt and crucible lie between 0.1 and 0.3, which is larger than desired but still very reasonably within the order of magnitude required for validity of the lumped capacitance assumption.

Special attention needs to be given to the frequent peaks in the Biot number of these two subunits. They occur when the predicted profiles of melt and crucible temperature cross each other, resulting in $(T_i - T_j)$ in Eq. 75 to become zero. Of the individual contributions to h_i^{eff}, this is caused by the radiation $\dot{q}_{1,2}^{\text{rad,encl}}$ within the enclosure, which is small compared to the melt/lid and the crucible/lid exchange. For this reason, the peaks are not taken as a reason to reject the lumped capacitance assumption.

Summary

In this article, a first-principles model of the mass and heat transfer in the effusion sources of a physical vapor deposition

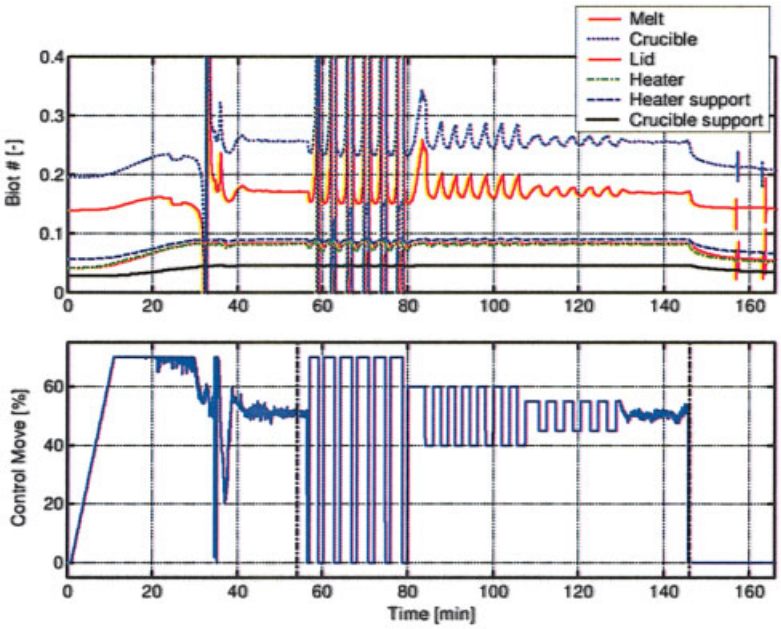

Figure 15. Biot number for evaluation experiment #1.

[Color figure can be viewed in the online issue, which is available at www.interscience.wiley.com]

process was developed. It includes models for the thermocouple and atomic absorption sensors. Model parameters were obtained from the literature and by a sequential parameter estimation that exploits the model structure. The model's consistency was crosschecked with experimental data different from the data that were used for the parameter estimation. Evaluation of the model is concluded by checking the consistency of the lumped capacitance assumption by computation of the Biot number. Considering the simplifications made in the model, prediction of both the static and the dynamic behavior in the high-temperature region is reasonable. The model thus provides the desired foundation for both simulation studies and model-based process control.

Acknowledgments

Funding from Global Solar Energy and the Delaware Research Partnership is gratefully acknowledged.

Literature Cited

1. Birkmire RW. Compound polycrystalline solar cells: Recent progress and Y2 K perspective. *Sol. Energy Mater. Sol. Cells.* 2001;65:17-28.
2. Birkmire RW, Eser E. Polycrystalline thin film solar cells: Present status and future potential. *Annu. Rev. Mater. Sci.* 1997;27:625-653.
3. Eisgruber IL, Joshi B, Gomez N, Britt J, Vincent T. In situ X-ray fluorescence used for real-time control of $Cu(In_xGa_{1-x})Se_2$ thin film composition. *Thin Solid Films.* 2002;408:64-72.
4. Junker ST, Birkmire RW, Doyle FJ III. Manufacture of thin-film solar cells: Modeling and control of $Cu(InGa)Se_2$ physical vapor deposition onto a moving substrate. *Ind. Eng. Chem. Res.* 2004;43:566-576.
5. Maissel LI, Glang R. *Handbook of Thin Film Technology*. New York, NY: McGraw-Hill; 1970.
6. Rocheleau RE, Baron BN, Russell TWF. Analysis of evaporation of cadmium sulfide for manufacture of solar cells. *AIChE J.* 1982;28: 656-661.
7. Kennard EH. *Kinetic Theory of Gases*. New York, NY: McGraw-Hill; 1938.
8. Hirschfelder JO, Curtiss CF, Bird RB. *Molecular Theory of Gases and Liquids*. New York, NY: Wiley; 1954.
9. Bird RB, Stewart WE, Lightfoot EN. *Transport Phenomena*. New York, NY: Wiley; 1960.
10. Brown GP, DiNardo A, Cheng GK, Sherwood TK. The flow of gases in pipes at low pressures. *J. Appl. Phys.* 1946;17:802-813.
11. Optimization Toolbox, *User's Guide*, Version 2. Natick, MA: The MathWorks; 2002.
12. Day RA, Underwood AL. *Quantitative Analysis*. 5th ed. Englewood Cliffs, NJ: Prentice-Hall; 1986.
13. Hanket GM. *Manufacture of Large Area Copper–Indium–Gallium–Diselenide Thin Films for Photovoltaic Applications*. PhD Thesis. Newark, DE: University of Delaware; 1999.
14. Incropera FP, DeWitt DP. *Fundamentals of Heat and Mass Transfer*. 4th ed. New York, NY: Wiley; 1981.
15. Cao Y, Faghri A. Heat transfer in liquid metals by natural convection. *Int. J. Heat Mass Transfer*. 1990;33:1367-1370.
16. Viskanta R, Kim DM, Gau C. Three-dimensional natural convection heat transfer of a liquid metal in a cavity. *Int. J. Heat Mass Transfer.* 1986;29:475-485.
17. Bergman TL, Webb BW. Simulation of pure metal melting with buoyancy and surface tension forces in the liquid phase. *Int. J. Heat Mass Transfer.* 1990;33:139-149.
18. Okano Y, Itoh M, Hirata A. Natural and Marangoni convections in a two-dimensional rectangular open boat. *J. Chem. Eng. Jpn.* 1989;22: 275-281.
19. Modest MF. *Radiative Heat Transfer*. New York, NY: McGraw-Hill; 1973.
20. *The Temperature Handbook*, Edition MM. Stamford, CT: Omega Engineering, Inc.; 2000.
21. Sandler SI. *Chemical and Engineering Thermodynamics*. 3rd ed. New York, NY: Wiley; 1998.
22. Dushman S. *Scientific Foundations of Vacuum Technique*. 2nd ed. New York, NY: Wiley ; 1962.
23. Lide DR, ed. *CRC Handbook of Chemistry and Physics*. 83rd ed. Boca Raton, FL: CRC Press; 2002.
24. Pauling L. *The Nature of the Chemical Bond and the Structure of Molecules and Crystals: An Introduction to Modern Structural Chemistry*. Ithaca, NY: Cornell Univ. Press; 1960.
25. Eggers DF Jr, Gregory NW, Halsey GD Jr, Rabinowitch BS. *Physical Chemistry*. New York, NY: Wiley; 1964.
26. Touloukian YS, Buyco EH. *Thermophysical Properties of Matter: Specific Heat—Metallic Elements and Alloys*. Vol 4. New York, NY: IFI/Plenum Data Corp.; 1970.
27. Touloukian YS, Buyco EH. *Thermophysical Properties of Matter: Specific Heat—Nonmetallic Solids*. Vol 5. New York, NY: IFI/Plenum Data Corporation, 1970.
28. *Using MATLAB*, Version 6. Natick, MA: The MathWorks; 2002.
29. Perry H, Green W. *Perry's Chemical Engineering Handbook*. 7th ed. New York, NY: McGraw-Hill; 1997.
30. Rohsenow WM, Hartnett JP. *Handbook of Heat Transfer*. New York, NY: McGraw-Hill; 1973.
31. Pierson HO. *Handbook of Carbon, Graphite, Diamond and Fullerenes: Properties, Processing and Applications*. Material Science and Process Technology Series. Park Ridge, NJ: Noyes Publications; 1993.
32. Touloukian YS, Powell RW, Ho CY, Klemens PG. *Thermophysical Properties of Matter: Thermal Conductivity—Metallic Elements and Alloys*. Vol 1. New York, NY: IFI/Plenum Data Corporation, 1970.
33. Sheppard RG, Mathes DM, Bray DJ, eds. *Properties and Characteristics of Graphite—For the Semiconductor Industry*. Decatur, TX: Poco Graphite, Inc.; 2001.
34. Touloukian YS, Powell RW, Ho CY, Klemens PG. *Thermophysical Properties of Matter: Thermal Conductivity—Nonmetallic Solids*. Vol 2. New York, NY: IFI/Plenum Data Corporation; 1970.
35. Tucker MK, Meyer DG. Nonlinear modeling, identification, and feedback control design for the modern effusion cell. *J. Vac. Sci. Technol. A.* 1998;16:3536-3553.
36. Åström KJ, Hägglund T. Automatic tuning of simple regulators with specifications on phase and amplitude margins. *Automatica*. 1984;20: 645-651.
37. Signal Processing Toolbox, User's Guide Version 6. Natick, MA: The MathWorks; 2002.
38. Sheela BV. An optimized step-size random search (OSSRS). *Comput. Methods Appl. Mech. & Eng.* 1979;19:99-106.
39. Junker ST. *Modeling and Control of a Continuous Thermo-Evaporation Process for Production of Thin-Film Photovoltaic Modules*. PhD Thesis. Newark, DE: University of Delaware; 2004.

Manuscript received Dec. 16, 2003, and revision received Jun. 15, 2004.